Journal of Metals, Materials and Minerals, 34(2), 1879, 2024

Corrosion behavior of YSZ and YSZ/NiCo coatings on inconel 625 exposed alkali chlorides

Resetiana Dwi DESIATI[1,*], Eni SUGIARTI[1], Bambang HERMANTO[1], Gerald Ensang TIMUDA[1], Hubby IZZUDDIN[1], Fraya Aulia SALSABILLA[2], and Anawati ANAWATI[3]

[1] *Research Center for Advanced Materials, National Research and Innovation Agency*
[2] *Department of Physics, Faculty of Science and Technology, Syarif Hidayatullah State Islamic University Jakarta,*
[3] *Department of Physic, Faculty of Mathematics and Natural Science, Universitas Indonesia*

***Corresponding author e-mail**: rese001@brin.go.id

Received date:
26 October 2023
Revised date
12 March 2024
Accepted date:
4 April 2024

Keywords:
YSZ;
Electrophoretic deposition;
Alkali chlorides;
Hot salt corrosion

Abstract

Alkali chloride attack on boiler pipe walls is considered the main problem of corrosion in the waste-to-energy (WTE) industry, even though uses superalloy. Electrophoretic deposited (EPD) yttria-stabilized zirconia (YSZ) coating is carried out to protect the Inconel 625 substrate. YSZ is deposited directly both on the Inconel 625 substrate and NiCo-Inconel 625. Corrosion resistance was conducted using the 3.5% NaCl electrochemical test and the hot salt corrosion test at 600°C in alkaline salt media such as NaCl, KCl, and $CaCl_2$. The potentiodynamic polarization curve shows that the YSZ coating deposited on the substrate (single-layer) has a corrosion rate of 0.065 $mm{\cdot}y^{-1}$, lower than that deposited on NiCo coating (double-layer). The double-layer, NiO_2 is formed in the NiCo layer due to the NaCl solution being trapped. Meanwhile, in hot salt corrosion at 600°C, $CaCrO_4$ is formed as a protective oxide layer. Furthermore, in the double-layer, an imperfect oxide layer is formed causing spallation and coating failure. The corrosion rate for single-layer hot salt corrosion for 40 h is 0.310 $mm{\cdot}y^{-1}$. As a result, the corrosion resistance of the single-layer is increased by the presence of the Cr_2O_3 oxide layer formed during sintering.

1. Introduction

Waste is an urgent matter in the world. Global waste can grow by up to 70% in 2050 as urbanization and population increase. (https://www.weforum.org/). Therefore, waste-to-energy (WTE) technology is increasingly being used to process waste into energy sources such as electricity or heat through combustion. However, burning waste can cause severe corrosion in boilers due to the presence of HCl and alkali salt contaminants as well as heavy metals in the waste [1]. The chemical attack caused by deposits that form on the walls of boiler pipes is considered to be the main cause of corrosion in the waste-to-energy (WTE) industry [2]. Conventional boilers are designed with high steam conditions ranging from 450°C to 540°C [3]. However, the WTE corrosion environment can become very aggressive when raising the vapor temperature above 500°C even for corrosion-resistant superalloys [4,5]. High corrosion rates occur especially when the deposit is melted [6]. Therefore we need a material as a boiler that is resistant to hot corrosion in extreme environments.

Ni-base alloys and coatings are widely accepted for increasing corrosion resistance at high temperatures, especially for protection in chlorinated environments [1]. However, coatings at high temperatures generally use ceramic as a constituent material. One of the ceramic materials often used is Yttria-Stabilized Zirconia (YSZ), which is zirconia stabilized by yttria.

YSZ ceramic coating is known for high-temperature applications such as the thermal barrier coating system (TBC system), also applied to fuel electrolyte cells [7,8] because it has low thermal conductivity, durability which is high enough to be able to withstand large loads, has a relatively small temperature gradient [9], and is resistant to corrosion [8].

Various methods are used to deposit YSZ ceramic coatings, including Air Plasma Spray (APS), High-Velocity Oxy Fuel (HVOF), Electron Beam Physical Vapor Deposition (EB-PVD), and Electrophoretic Deposition (EPD). EPD is considered a method with good universality for different materials and can adapt complex structures with simple equipment [10] and short coating times.

Therefore, this study studied YSZ coating with electrophoretic deposition method which was deposited directly on Inconel 625 substrate compared to YSZ coating which is deposited on NiCo coating with Inconel 625 substrate for corrosion resistance in extreme salt environments with a mixture of NaCl, KCl, and $CaCl_2$ at 600°C. Potential Dynamic Polarization (PDP) test at 3.5% NaCl to determine the coating performance. NiCo bond coat was chosen because adding cobalt to nickel can increase corrosion resistance. After all, it has good adhesion with the formation of a passive layer of NiO or $Ni(OH)_2$ on the surface [11]. In addition, previous research found that Nickel coating with the addition of Co can increase its hardness.

2. Experimental

2.1 Sample preparation

Inconel 625 with dimensions 15 mm × 15 mm × 1.2 mm as substrate. The substrate was polished using various grits of SiC paper for up to #1200**.** Then the preparation is continued by cleaning and degreasing the substrate into DI water and acetone in an ultrasonic bath for 180 s. In this study, the NiCo coating for the bond coat used the electroplating method and the YSZ coating used the electrophoretic deposition (EPD) method. Ni - 5% Co was electro-plated using Ni-strike solution for 20 s and Ni-watt solution for 2 h with a current density of 20 $A{\cdot}cm^{-2}$. The composition of Ni-strike solutions and Ni-watts has been described in previous publications [12]. Whereas, the YSZ solution has also been described elsewhere, which uses 3YSZ powder (3 mol% Y_2O_3, > 99%, Kanto, Japan) [13]. The EPD process and the sintering method used the gradient method, 20 V fo 60 V for 12 min for EPD and 750°C followed by 1200°C each held for 2 h for sintering. After the electroplating process is followed by the EPD process, this coating is called a double-layer. As a comparison, the substrate was directly coated with the EPD process, hereinafter referred to as a single-layer. Hot corrosion testing was carried out by burying samples in silica sand with the addition of NaCl 0.4 wt%, KCl 0.4 wt%, and $CaCl_2$ 0.2 wt%. Pure water was added to the mixed salt, then milled for 5 h at a speed of 100 rpm, then dried using a hot plate.

2.2 Testing and characterization

To determine the corrosion resistance of the double and single-layers that have been formed, corrosion testing was carried out in a mixed salt environment of NaCl, KCl, and $CaCl_2$ at 600°C for 40 h. The corrosion rate was calculated by weight loss method, with the Equation:

$$CR = \frac{K \times W}{D \times A \times T}$$

CR: Corrosion Rate ($mm{\cdot}y^{-1}$)
K: Constant (8.76×10^4)
W: Mass loss (mg)
D: Density ($g{\cdot}cm^{-3}$)
A: Exposed area (cm^2)
T: Time of exposure (h)

An electrochemical test was carried out in 3.5% NaCl solution at room temperature. Three electrode cells were used for measurements. The Ag/AgCl is the reference electrode, platinum is the counter electrode, and samples are the working electrode. The potentiodynamic polarization was acquired for ±250 mV potential range and at a scan rate of 0.1 $mV{\cdot}s^{-1}$. Rate and potential corrosion were obtained through Tafel extrapolation using the Zive-5 Instrument. The equivalent weight (EW) of single-layer and double-layer samples used was 25.57 $g{\cdot}eq^{-1}$, and 27.96 $g{\cdot}eq^{-1}$, respectively. The density of the single-layer and double-layer used 8.44 $g{\cdot}cm^{-3}$, and 8.9 $g{\cdot}cm^{-3}$, respectively.

The microstructure before and after corrosion was evaluated using a field emission scanning electron microscope (FESEM JEOL, JIB4610F), element distribution using an energy dispersive X-ray spectroscope (EDX detector, Oxford, X-MAX50), phase identification using Cu-Kα radiation, wavelength, 1.5405 Å for 2θ from 10° to 90° (Rigaku SmartLab).

3. Results and discussion

3.1 Phase composition and microstructure before corrosion

Figure 1 shows the single and double-layer sample's X-ray diffraction patterns after sintering. Both samples were detected as monoclinic and tetragonal ZrO_2 phases. A monoclinic percentage of 65 ± 4% and 35 ± 4% tetragonal. In the double-layer, around 9% of the nickel phase is detected. The transition from a raw powder or a green body which is mainly tetragonal to mainly monoclinic can have negative effects on zirconia restorations [13,14]. The monoclinic phase is considered to hurt the tolerance of the Thermal Barrier Coating due to microcracking caused by the volume expansion from the t-m transformation during heating and cooling [15]. The addition of 3 mol% yttria is not sufficient to stabilize the t-ZrO_2 phase during sintering above 1000°C, where temperature changes are the dominant factor that can cause phase transformation in this coating.

It has been suggested that YSZ undergoes spinodal decomposition of Y-depleted material after sintering [16]. Yttria in YSZ serves to stabilize the tetragonal phase. Undoped zirconia has a monoclinic structure, but with yttria doping, it becomes a tetragonal or cubic structure [17,18]. The yttria (Y_2O_3) dopant precipitates in the nanoscale region within the tetragonal matrix, which cannot be detected by X-ray diffraction due to its small size [16].

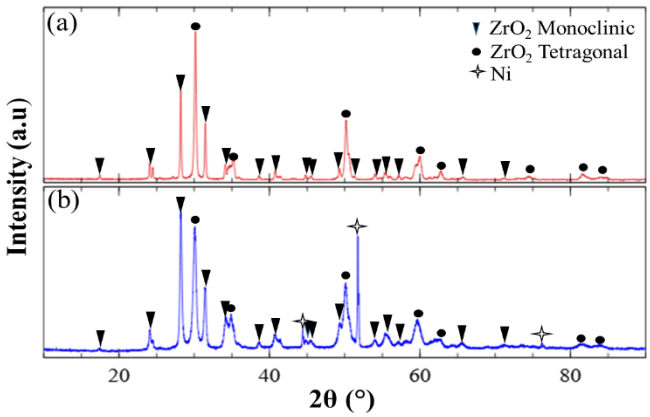

Figure 1. Diffraction patern after sintering 1200°C (a) single-layer, and (b) double-layer.

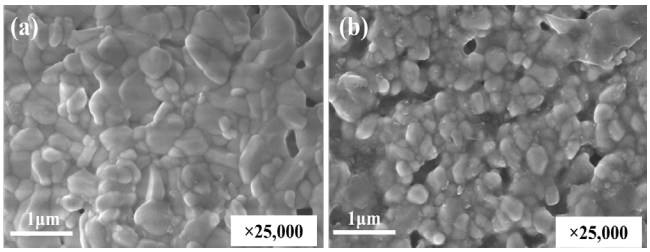

Figure 2. Surface microstructure (a) single-layer, (b) double-layer.

Figure 2 shows the surface microstructure of single-layer (Figure 2(a)) and double-layer (Figure 2(b)). The grain size of the double-layer looks smaller than the single-layer. In calculations using image J, the grain size of the double-layer averages around 0.32 µm, and the single-layer reaches 0.46 µm. Double-layer and single-layer porosity are 2.3% and 1.9%, respectively. Possibly due to the higher porosity, this causes the Ni phase in the double-layer to be detected by X-ray diffraction even though it is low.

The EPD process involves the attraction and deposition of charged particles dispersed in a liquid medium onto a conductive substrate, due to the flowing DC electric current [19]. The electrophoretic movement of particles stops by the substrate, and the particle density continues to increase there due to accumulation [19]. When using the gradient method in the EPD process, small particles usually deposit at a lower voltage, followed by large particles deposit as the voltage increases [20]. When the electrical conductivity of the substrate is high, the current density becomes higher, forming a potential for gradient deposition at the start of the coating to occur more quickly. As the deposition time increases, at the end of the EPD, the current density becomes lower due to the increasing thickness of the deposited layer, which acts as a resistance layer too quickly [21]. This has the potential for double-layer samples which have a smaller grain size and are porous on the surface, caused by a faster decrease in current density at the end of deposition because the YSZ coating is deposited on top of the NiCo coating which is more conductive than Inconel 625.

Figure 3 In the elemental line analysis, it is clear that the chromium oxide (Cr_2O_3) layer is formed in the single-layer sample due to sintering. The formation of Cr_2O_3 is certainly very beneficial because this layer can function to increase corrosion resistance. The double-layer does not form a thermally grown oxide (TGO) as in the single-layer, although it is already visible that there is diffusing outward of the Cr element from the substrate to NiCo coating. Even though the YSZ layer in the double-layer sample has a higher porosity, allowing more oxygen to diffuse into the layer, the presence of a NiCo coating with a thickness of approximately 60 µm prevents the diffusion of oxygen to Inconel substrate, so that the Cr_2O_3 layer is not formed like in the single-layer sample, where the Cr element in the Inconel composition diffusing outward and reacted with oxygen to form Cr_2O_3.

The chemical composition of Inconel 625 shown [22] in the Table 1.

HSC Chemistry Software version 9.8.1.2 [23] is used to confirm the Gibbs free energy (ΔG) at a temperature of 1200°C is as follows:

$$2\ Ni_{(s)} + O_{2(g)} \rightarrow 2\ NiO_{(s)}, \quad \Delta G = -215{,}755\ kJ \quad (1)$$

$$2\ Cr_{(s)} + 1{,}5\ O_{2(g)} \rightarrow Cr_2O_{3(s)}, \quad \Delta G = -758.578\ kJ \quad (2)$$

$$2\ Fe_{(s)} + 1.5\ O_{2(g)} \rightarrow Fe_2O_{3(s)}, \quad \Delta G = -443.567\ kJ \quad (3)$$

$$Mo_{(s)} + O_{2(g)} \rightarrow MoO_{2(s)}, \quad \Delta G = -326.566\ kJ \quad (4)$$

$$Nb_{(s)} + O_{2(g)} \rightarrow NbO_{2(s)}, \quad \Delta G = -537.160\ kJ \quad (5)$$

$$2\ Al_{(s)} + 1.5\ O_{2(g)} \rightarrow Al_2O_{3(s)}, \quad \Delta G = -1205.414\ kJ \quad (6)$$

Even though ΔG Al_2O_3 is more negative than Cr_2O_3, Cr growth is faster because the composition of Cr is much more than Al in Inconel 625, consequently promoting Cr_2O_3 formation instead of Al_2O_3 as a TGO layer in a single-layer system.

Table 1. Chemical composition of Inconel 625.

Element	%
Nickel	58.0 min.
Chromium	20.0 to 23.0
Iron	5.0 max.
Molybdenum	8.0 to 10.0
Niobium (plus Tantalum)	3.15 to 4.15
Carbon	0.10 max.
Manganese	0.50 max.
Silicon	0.50 max.
Phosphorus	0.015 max.
Sulfur	0.015 max.
Aluminum	0.40 max.
Titanium	0.40 max.
Cobalt[a]	1.0 max.

[a]If determined

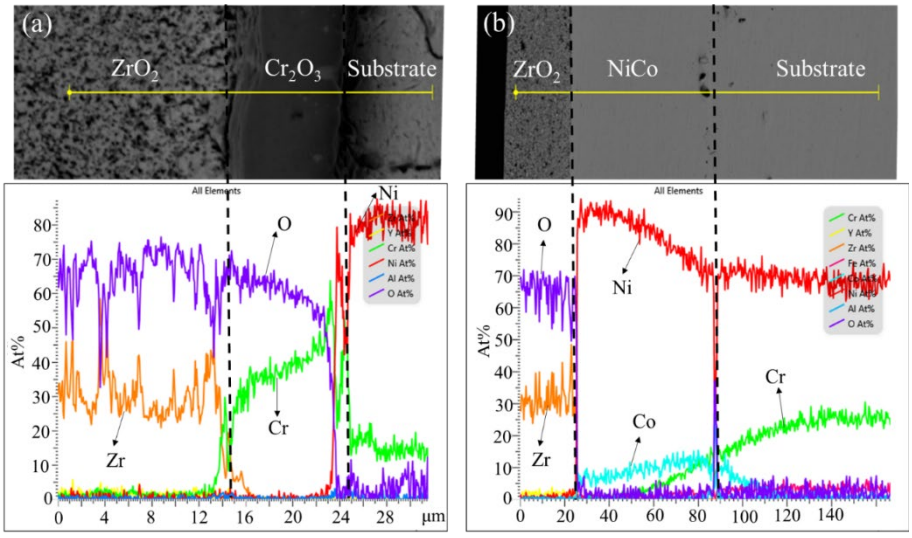

Figure 3. Elemental line analysis (a) single-layer, and (b) double-layer.

3.2 Electrochemical test

3.2.1 Potentiodynamic polarization

Figure 4 The Potentiodynamic curve of the single-layer and the double-layer, from the potentiodynamic curve, the corrosion parameters such as anodic Tafel slope (βa), cathodic Tafel slope (βc), corrosion potential (Ecorr), corrosion current density (Jcorr) and corrosion rate (CR) were determined using the Tafel extrapolation method. The results as presented in Table 2. Where single and double layer, 0.065 mm·y^{-1} and 0.105 mm·y^{-1}, respectively. This is the possibility of diffusion of ions from NaCl through the pores of the surface of ZrO_2 coating in the double-layer and then trapped in the NiCo coating, resulting in local corrosion of the layer. It is different in the single-layer where the ions from NaCl that enter through the pores of the ZrO_2 surface layer are blocked by the Cr_2O_3 oxide layer, making it difficult to react with NaCl at room temperature conditions. The Gibbs free energy (ΔG) Cr_2O_3 with NaCl at 873 K is 176 kJ·mol^{-1} as in a study conducted by Hiraide, 2009 [24]. This shows that metal reduction is difficult because of the presence of Cr_2O_3 which can counteract the diffusion of Na^+ and Cl^- ions into the substrate.

3.2.2 Microstructure after electrochemical at 3.5% NaCl

Figure 5 shows the cross-section after the potentiodynamic polarization test. It shows that in the single-layer there is no change, it's just that the layer above is visible, it is a silver paste that is used as a conductor for electrochemical tests. In the double-layer, it is seen that there is a layer that is thought to be NaO_2 which is probably formed from the result of the NaCl reaction in the form of a solution as in reactions 7 to 9, trapped in the NiCo layer, which causes local corrosion of the NiCo coating. In the potentiodynamic polarization test, the water in the electrolyte breaks down which causes the evolution of oxygen, where the water can decompose and release oxygen [25,26].

$$NaCl_{(s)} + H_2O_{(l)} \rightarrow Na^+_{(aq)} + Cl^-_{(aq)} \quad (7)$$

$$2H_2O_{(l)} \rightarrow 4H^+_{(aq)} + O_{2(g)} + 4e^- \quad (8)$$

$$Na^+_{(aq)} + O_{2(g)} \rightarrow NaO_{2(s)} \quad (9)$$

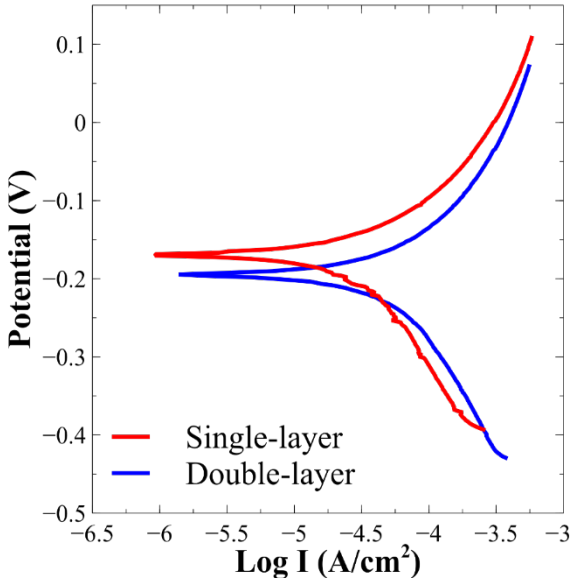

Figure 4. Potentiodynamic curve of single and double-layer.

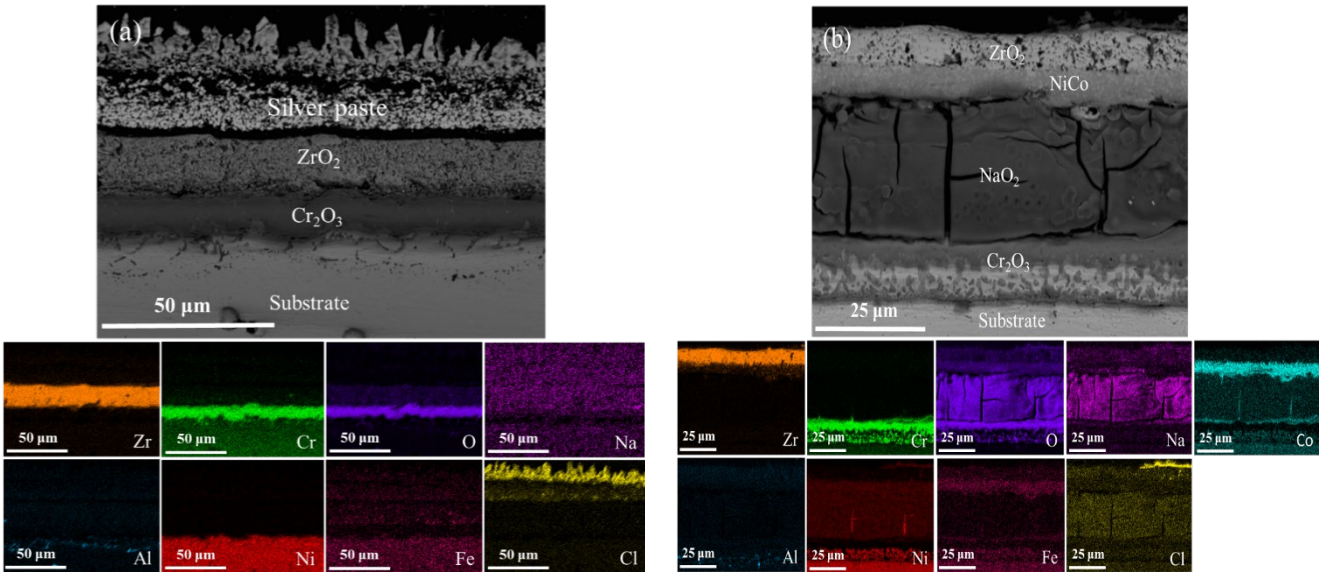

Figure 5. Cross-section and EDS mapping FE-SEM image after potentiodynamic polarization test (a) single-layer, and (b) double-layer.

Table 2. Corrosion parameters resulting from the Tafel extrapolation method.

Coating	E_{corr} (mV)	j_{corr} (µA·cm^{-2})	β_{anodic} (mV)	$\beta_{cathodic}$ (mV)	CR (mmpy)
Single-layer (YSZ)	–166.35	6.60	35.45	57.50	0.065
Double-layer (YSZ/NiCo)	–194.08	10.18	40.97	48.79	0.105

Figure 6 shows the line analysis of the double-layer, it can be seen that there is a reduction in Co elements in the NiCo coating. The more negative reduction potential will corrode preferentially to the nobler or higher reduction potential metal, the Co is 0.03 V more negative than Ni, where Ni is about –0.25 V and Co –0.28 V. In an electrolyte environment, the Cr element that diffuses from the substrate as seen in Figure 3(b), forms Cr ions as in reaction 10, then reacts with oxygen to form a Cr_2O_3 layer as in reaction 11. So in the double-layer, a layer is seen that is thought to be Cr_2O_3 which can be seen in the cross-section EDS mapping FE-SEM Figure 5(b).

$$Cr_{(s)} \rightarrow Cr^{3+}_{(aq)} + 3e^- \quad (10)$$

$$2Cr^{3+}_{(aq)} + 4.5O_{2(g)} \rightarrow 3Cr_2O_{3(s)} \quad (11)$$

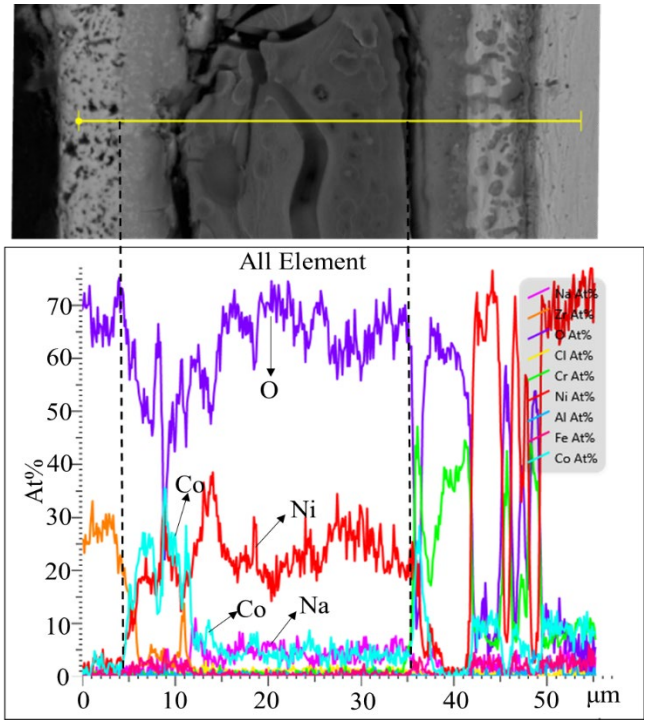

Figure 6. Elemental line analysis of double-layer after potentiodynamic polarization test.

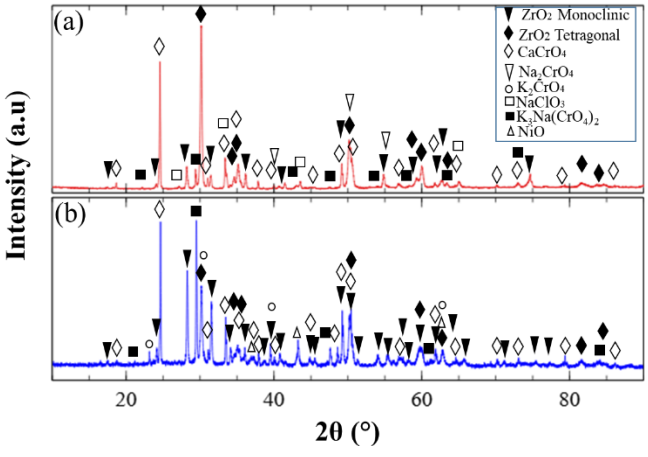

Figure 7. X-ray diffraction after hot salt corrosion (a) single-layer, and (b) double-layer.

3.3 Phase composition and microstructure after hot corrosion

Figure 7 Shows XRD after hot salt corrosion, ZrO_2 monoclinic and tetragonal phases are still detected which showed that zirconia was able to act as a barrier and was difficult to react with salt at a temperature of 600°C. However, Cr_2O_3 reacts very easily with $CaCl_2$ to form $CaCrO_4$, as reported by S. Karlsson, 2016, $CaCl_2$ used as a corrosive agent is very fast to form CaO at a temperature of 600°C, Ca element also very easily reacts with Cr element [27].

The reaction that occurs is shown in the reaction Equation (12) and Equation (13).

$$2CaCl_{2(s)} + O_{2(g)} \rightarrow 2CaO_{(s)} + 2Cl_{2(g)} \quad (12)$$

$$2CaO_{(s)} + Cr_2O_{3(s)} + 1.5O_{2(g)} \rightarrow 2CaCrO_{4(s)} \quad (13)$$

In addition, it was detected as $K_3Na(CrO_4)_2$, K_2CrO_4, Na_2CrO_4, $NaClO_3$, and NiO phases. Reaction Equation (14-18) show the reactions that occurred.

$$2CaO_{(s)} + Cr_2O_{3(s)} + 1.5O_{2(g)} \rightarrow 2CaCrO_{4(s)} \quad (14)$$

$$Cr_2O_{3(s)} + 4NaCl_{(s)} + 2.5O_{2(g)} \rightarrow 2Na_2CrO_{4(s)} + 4Cl_{2(g)} \quad (15)$$

$$3K_2CrO_{4(s)} + Na_2CrO_{4(s)} \rightarrow 2K_3Na(CrO_4)_{2(s)} \quad (16)$$

$$NaCl_{(s)} + 1.5O_{2(g)} \rightarrow NaClO_{3(s)} \quad (17)$$

$$2Ni_{(s)} + O_{2(g)} \rightarrow 2NiO_{(s)} \quad (18)$$

However, the phases detected on the surface area as seen in Figure 8 are not evenly distributed.

In contrast to $CaCrO_4$ which is in the form of a layer. The $CaCrO_4$ protective layer formed on single and double-layer surfaces. $CaCrO_4$ has the same melting point as ZrO_2 which is about 2700°C. So it is possible to be able to inhibit corrosion. However, in the double-layer, when viewed from the corrosion rate, the corrosion of hot salt for 40 h was higher than that of the single-layer, namely 1.725 $mm \cdot y^{-1}$ and 0.310 $mm \cdot y^{-1}$ respectively. This is calculated as mass loss up to 40 h as in the mass reduction curve in Figure 9.

It turns out that the SEM cross-section (Figure 10) shows that the double-layer sample after hot salt corrosion (Figure 10(b)) is a very complex layer. The EDS confirmed the oxide scale of Cr_2O_3 and Al_2O_3 layers had not formed completely and that there are gaps along the interface area which can cause coating spallation. During the initial hot salt corrosion, Cr_2O_3 oxide is formed, then reacts quickly with Ca to form $CaCrO_4$, due to the sluggish diffusion of Al from the substrate to the surface. Although Al exhibits higher reactivity towards oxygen compared to Cr and Ni, its diffusion rate is not sufficient to sustain the exclusive formation of the α-Al_2O_3 scale [28]. The $CaCrO_4$ is only found above the NiCo coating.

This is different from the case of the single-layer sample (Figure 10(a)) where $CaCrO_4$ is formed and replaces the position of the Cr_2O_3 oxide layer that was formed before hot salt corrosion. $CaCrO_4$ is also found in the surface layer and between layers of peeled ZrO_2 to protect against further corrosion. $CaCrO_4$ is an inhibite corrosion [29].

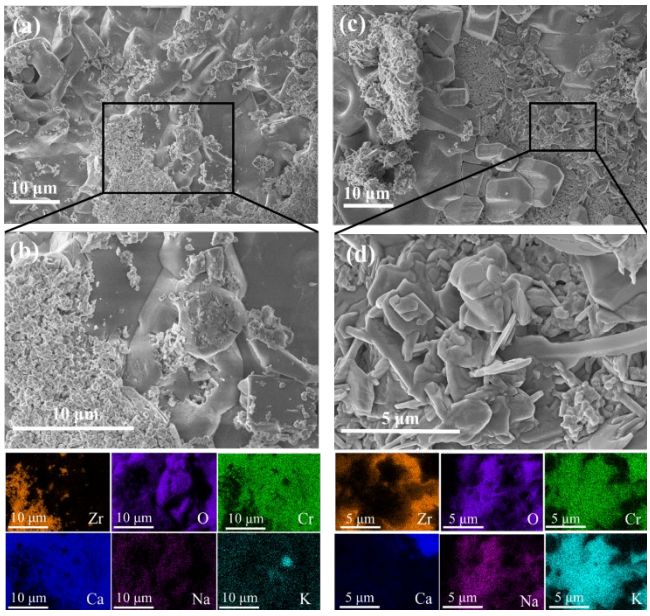

Figure 8. Surface microstructure and EDS mapping FE-SEM image after of hot salt corrosion (a),(b) single-layer, and (c),(d) double-layer.

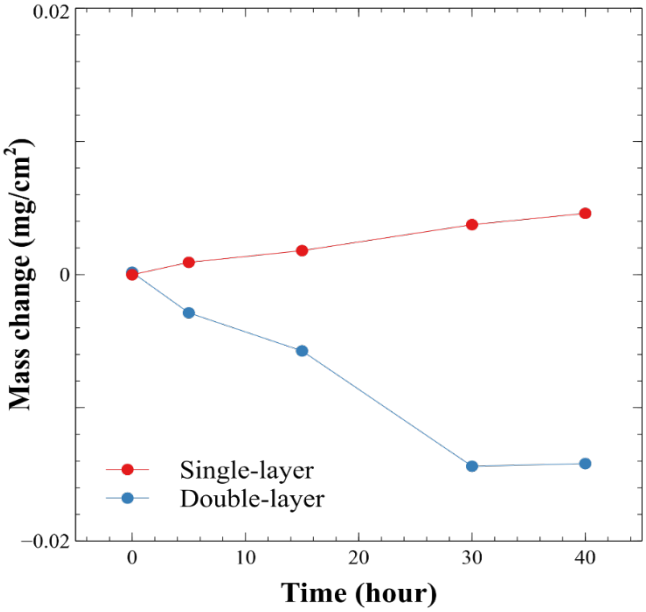

Figure 9. Mass change curve after hot salt corrosion

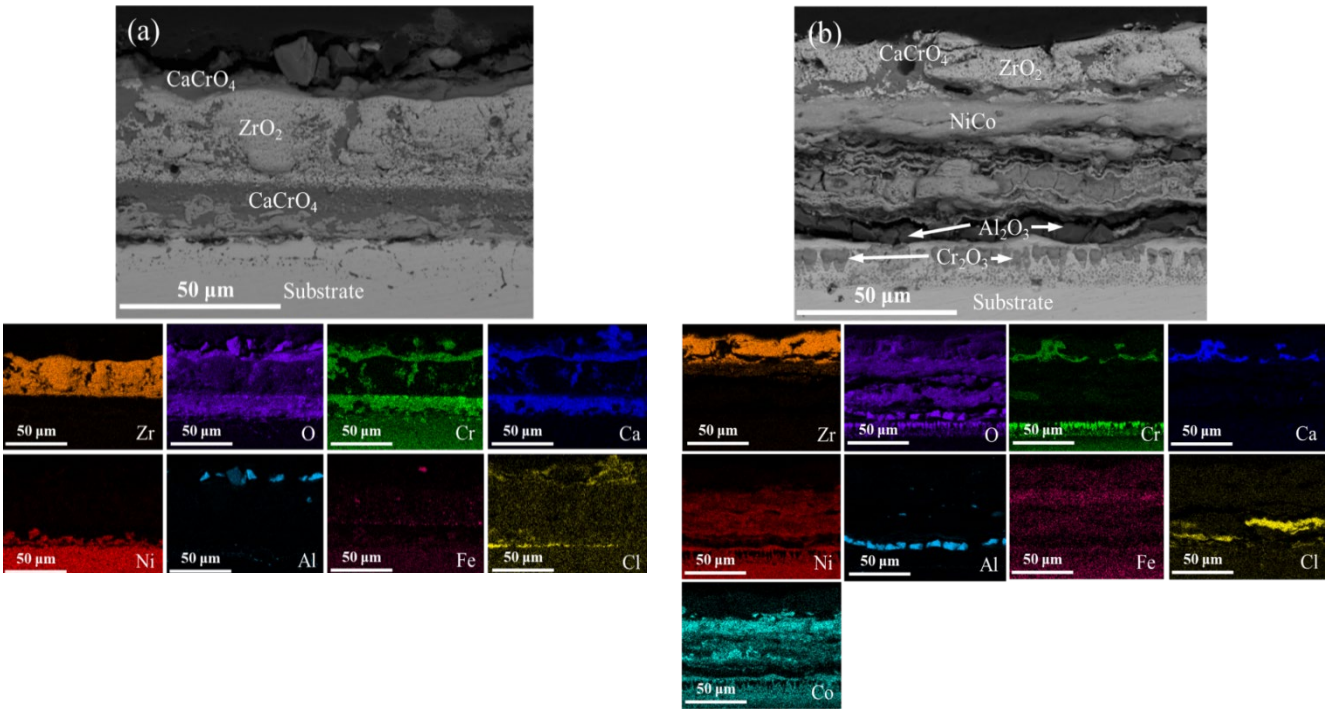

Figure 10. Cross-section and EDS mapping FE-SEM image after hot salt corrosion 40 h (a) single-layer, and (b) double-layer.

4. Conclusions

The corrosion behavior of YSZ (single-layer) and YSZ/NiCo (double-layer) layers deposited on Inconel 625 has been studied. In the electrochemical test of 3.5% NaCl, the corrosion rate of the single-layer was 0.065 mm·y^{-1}, lower than the double-layer, this happened because the double-layer corrosion had occurred in the NiCo layer and formed NiO_2 which was caused by the NaCl solution diffusing and being trapped in the NiCo layer. In hot salt corrosion at 600°C with NaCl, KCl, and $CaCl_2$ media for 40 h, a protective oxide layer of $CaCrO_4$ is formed on both of them, due to a reaction of Cr_2O_3 and CaO, where $CaCl_2$ easily forms CaO at a temperature of 600°C. In the single-layer, the corrosion rate based on mass loss is 0.310 mm·y^{-1} which is lower than the double-layer. In the double-layer, spallation and layer failure occur because the Cr_2O_3 and Al_2O_3 oxide layers that are formed are incomplete and form gaps along the interface area.

Acknowledgements

The authors would like to thank the Research Center for Advanced Materials (PRMM), National Research and Innovation Agency (BRIN) for providing processing and characterization facilities. The authors acknowledge the financial support from Rumah Program Nanoteknologi dan Material Maju B-5628/III.10.1/HK.01.00/4/2022 No.51.

References

[1] H. Izzuddin, S. Hayashi, S. Yoneda, T. Kogin, E. Ishikawa, and M. Noguchi, "Effect of Mo on corrosion behavior of $Ni_20Cr–xMo$ alloys in air with NaCl–KCl–$CaCl_2$ vapor at 570°C," *Materials and Corrosion*, vol. 71, no. 9, pp. 1488-1499, 2020.

[2] J. Liu, D. Dyson, and E. Asselin, "Long-term hot corrosion behavior of boiler tube alloys in waste-to-energy plants," *Oxidation of Metals*, vol. 86, no. 1-2, pp. 135-149, 2016.

[3] G. Sorell, "The role of chlorine in high temperature corrosion in waste-to-energy plants," *Materials at High Temperatures*, vol. 14, no. 3, pp. 207-220, 1997.

[4] N. Otsuka, "A thermodynamic approach on vapor-condensation of corrosive salts from flue gas on boiler tubes in waste incinerators," *Corrosion Science*, vol. 50, no. 6, pp. 1627-1636, 2008.

[5] S.-H. Lee, N. J. Themelis, and M. J. Castaldi, "High-temperature corrosion in waste-to-energy boilers," *Journal of Thermal Spray Technology*, vol. 16, no. 1, pp. 104-110, 2007.

[6] M. Sánchez Pastén, and M. Spiegel, "High temperature corrosion of metallic materials in simulated waste incineration environments at 300–600°C," *Materials and Corrosion*, vol. 57, no. 2, pp. 192-195, 2006.

[7] L. B. Chen, "Yttria-stabilized zirconia thermal barrier coatings - A review," *Surface Review and Letters*, vol. 13, no. 05, pp. 535-544, 2006.

[8] X. Q. Cao, R. Vassen, and D. Stoever, "Ceramic materials for thermal barrier coatings," *Journal of the European Ceramic Society*, vol. 24, no. 1, pp. 1-10, 2004.

[9] N. P. Padture, M. Gell, and E. H. Jordan, "Thermal barrier coatings for gas-turbine engine applications," *Science*, vol. 296, no. 5566, pp. 280-284, 2002.

[10] M. Bai, F. Guo, and P. Xiao, "Fabrication of thick YSZ thermal barrier coatings using electrophoretic deposition," *Ceramics International*, vol. 40, no. 10, pp. 16611-16616, 2014.

[11] K. Sharifi and M. Ghorbani, "Corrosion behaviour of Ni–Co alloy coatings at Kish Island (Marine) atmosphere," *Bulletin of Materials Science*, vol. 37, no. 3, pp. 713-719, 2014.

[12] E. Sugiarti, R. D. Desiati, K. A. Zaini, K. Hartanto, and N. Prastomo, "Effect of Co concentration on hardness of NiCo coating layer synthesized by electroplating method," *Journal of Physics: Conference Series*, vol. 1191, p. 012062, 2019.

[13] R. D. Desiati, A. Anawati, and E. Sugiarti, "Two-step sintering improved compaction of electrophoretic-deposited YSZ coatings," *Journal of Materials Engineering and Performance*, vol. 31, no. 12, pp. 9888-9899, 2022.

[14] T. J. Lucas, N. C. Lawson, G. M. Janowski, and J. O. Burgess, "Effect of grain size on the monoclinic transformation, hardness, roughness, and modulus of aged partially stabilized zirconia," *Dental Materials*, vol. 31, no. 12, pp. 1487-1492, 2015.

[15] S. E. Redfern, R. W. Grimes, and R. D. Rawlings, "The hydroxylation of t-ZrO_2 surfaces," *Journal of Materials Chemistry*, vol. 11, no. 2, pp. 449-455, 2001.

[16] B. Butz, R. Schneider, D. Gerthsen, M. Schowalter, and A. Rosenauer, "Decomposition of 8.5 mol.% Y_2O_3-doped zirconia and its contribution to the degradation of ionic conductivity," *Acta Materialia*, vol. 57, no. 18, pp. 5480-5490, 2009.

[17] H. Hayashi, T. Saitou, N. Maruyama, H. Inaba, K. Kawamura, and M. Mori, "Thermal expansion coefficient of yttria stabilized zirconia for various yttria contents," *Solid State Ionics*, vol. 176, no. 5-6, pp. 613-619, 2005.

[18] M. Yashima, K. Ohtake, H. Arashi, M. Kakihana, and M. Yoshimura, "Determination of cubic-tetragonal phase boundary in $Zr_{1-X}Y_XO_{2-X/2}$ solid solutions by Raman spectroscopy," *Journal of Applied Physics*, vol. 74, no. 12, pp. 7603-7605, 1993.

[19] P. Amrollahi, J. S. Krasinski, R. Vaidyanathan, L. Tayebi, and D. Vashaee, "Electrophoretic deposition (EPD): Fundamentals and applications from nano- to microscale structures," in *Handbook of Nanoelectrochemistry*, M. Aliofkhazraei and A. S. H. Makhlouf, Eds. Cham: Springer International Publishing, 2016, pp. 561-591.

[20] R. D. Desiati, A. Anawati, and E. Sugiarti, "Microstructural and mechanical characteristic of ceramic composite coating developed by electrophoretic deposition," *IOP Conference Series: Materials Science Engineering*, vol. 1098, no. 6, p. 062073, 2021.

[21] H. Negishi, K. Yamaji, N. Sakai, T. Horita, H. Yanagishita, and H. Yokokawa, "Electrophoretic deposition of YSZ powders for solid oxide fuel cells," *Journal of Materials Science*, vol. 39, no. 3, pp. 833-838, 2004.

[22] "Data Sheet Inconel 625." www.specialmetals.com, 13-Aug-2013.

[23] "HSC Chemistry Software." Outotec (Finland) Oy, 2019.

[24] N. Hiraide, T. Muneno, and H. Kajimura, "Reaction of Cr and Cr oxide with NaCl at elevated temperature," *Zairyo-to-Kankyo*, vol. 58, no. 10, pp. 348-355, 2009.

[25] S. Esmailzadeh, M. Aliofkhazraei, and H. Sarlak, "Interpretation of Cyclic potentiodynamic polarization test results for study of corrosion behavior of metals: A Review," *Protection of Metals and Physical Chemistry of Surfaces*, vol. 54, no. 5, pp. 976-989, 2018.

[26] E. McCafferty, *Introduction to Corrosion Science*. New York, NY: Springer New York, 2010.

[27] S. Karlsson, J. Pettersson, L.-G. Johansson, and J.-E. Svensson, "Alkali induced high temperature corrosion of stainless steel: The influence of NaCl, KCl and $CaCl_2$," *Oxidation of Metals*, vol. 78, no. 1-2, pp. 83-102, 2012.

[28] H. Shahbazi, H. Vakilifard, R. B. Nair, A. C. Liberati, R. S. Lima, P. Stoyanov, and C. Moreau, "High entropy alloy bond coats for thermal barrier coatings: A review," *Journal of Thermal Spray Technology*, vol. 33, no. 10, 2023.

[29] Centre international de recherche sur le cancer, Ed., *A review of human carcinogens*. Lyon: International agency for research on cancer, 2012.